



Rock Anelasticity, Pore Geometry and the Biot–Gardner Effect

Wei Cheng¹ · José M. Carcione^{1,2} · Ayman N. Qadrouh³ · Mamdoh Alajmi³ · Jing Ba¹

Received: 26 August 2019 / Accepted: 20 May 2020
© Springer-Verlag GmbH Austria, part of Springer Nature 2020

Abstract

The anelastic properties of porous rocks depend on the pore characteristics, specifically, the pore aspect ratio and the pore fraction (related to the soft porosity). At high frequencies, there is no fluid pressure communication throughout the pore space and the rock becomes stiffer than at low frequencies, where the pore pressure is fully equilibrated. The models considered here include explicit pore geometry information in determining the poroelastic parameters. They are extensions of the EIAS (equivalent inclusion-average stress) and CPEM (cracks and pores effective medium) models to the whole frequency range, based on the Zener model. Knowing the degree of stiffness dispersion between the low- and high-frequency limits, we fit experimental data in the whole frequency range and obtain the average crack aspect ratio and soft porosity as a function of effective pressure. Then, we compute the dispersion and quality factor of the bulk, shear and Young moduli, and the P- and S-wave seismic velocities and quality factors as a function of frequency. However, when measuring axial or volumetric motions along a cylindrical sample, there is fluid flow at the ends of the sample in the experiments considered here. This generates dispersion and attenuation due to axial flow of the pore fluid, which does not occur for a plane wave in unbounded media. This phenomenon is called “drained/undrained transition” Pimienta et al. (J Geophys Res Solid Earth; <https://doi.org/10.1002/2017JB014645>, 2017). Actually, it is an axial version of the Biot–Gardner (BG) effect, and implies an “artificial” (mesoscopic) attenuation peak (and dispersion) due to the generation of slow (diffusion) Biot modes at the cylinder boundary, inducing a global flow at the scale of the sample. The classical BG effect is due to fluid flow along the radial direction, on the basis of open-pore conditions at the sides of the sample. In this case, the sides are sealed. To use the EIAS and CPEM models, the BG effect has to be removed to obtain the intrinsic Q of the rock. The models are applied here for measurements on sandstone. The axial BG effect is more evident if the intrinsic attenuation is weak or absent. An example is Lavoux limestone, which has a bimodal porosity distribution, with an equal proportion of intragranular microporosity and intergranular macroporosity (round pores). In this case, the attenuation and dispersion are related to the BG effect, since no squirt flow is detected due to the absence of cracks. We verified that the bulk and Young moduli obtained from the axial and hydrostatic oscillations are consistent with each other, and that the theoretical description of the axial BG effect shows some discrepancies with the data.

Keywords Anelasticity · Dispersion · Attenuation · Crack aspect ratio · Soft porosity · Biot–Gardner effect

1 Introduction

Wave propagation in porous saturated rocks shows anelastic properties, namely, velocity and stiffness dispersion and dissipation of energy depending on frequency (e.g., Jones 1986; Carcione 2014; Zhang et al. 2019). Anelasticity has gained much attention in recent years from a practical point of view. The applications cover a variety of fields, including physics and geophysics, engineering and soil mechanics, underwater acoustics, etc. In particular, in the exploration of oil and gas reservoirs, it is important to predict the rock porosity, permeability and the presence of fluids (type and saturation). These

✉ Jing Ba
jba@hhu.edu.cn

¹ School of Earth Sciences and Engineering, Hohai University, Nanjing 211100, China

² Istituto Nazionale di Oceanografia e di Geofisica Sperimentale (OGS), Borgo Grotta Gigante 42c, 34010 Sgonico, Trieste, Italy

³ KACST, PO Box 6086, Riyadh 11442, Saudi Arabia

microstructural properties and in situ rock conditions can be obtained, in principle, from seismic properties, such as wave velocity and attenuation (Müller et al. 2010; Carcione et al. 2010).

At seismic frequencies, Gassmann equation describes the wave velocities, but this model does not include the explicit dependence of the elastic behaviour on pore structure, basically, crack aspect ratio and density (soft porosity), and cannot predict the high-frequency behaviour. Soft or crack porosity is very sensitive to effective pressure (lithostatic minus pore) and greatly affects the rock stiffnesses, unlike equant or stiff porosity, which occupies almost all the pore space. To describe the stiffness and velocity dispersions and dissipation factor as a function of frequency, including the rock microstructure, we consider the EIAS model (Benveniste 1987; Endres and Knight 1997). This model is consistent with the Gassmann equation at low frequencies and with the Hashin–Shtrikman bounds when applied to two-phase systems regardless of the pore shape spectrum. This model is a generalization of that from Budiansky and O’Connell (1980), based on the model of Kuster and Tököz (1974). To verify the robustness of the EIAS model, we also consider the model developed by Adelinet et al. (2011) (CPEM), based on a different approach. This model also consists on an isotropic distribution of spherical pores or elliptical cracks. They compared the theoretical predictions with the data obtained on a basaltic rock and found a good agreement.

We consider three fully saturated rock samples, namely, Lavoux limestone (Borgomano et al. (2017)), and Wilkenson and Bentheim sandstones (Pimienta et al. 2017). The fit of experimental data at the relaxed and unrelaxed states for the sandstones allows us to obtain the crack aspect ratio and fraction (soft porosity); while the frequency dependence of the moduli, phase velocities and quality factors are described by a Zener model (e.g., Carcione 2014). Due to the measurement procedure used by Pimienta et al. (2017), there is an attenuation mechanism (relaxation peak) related to the geometry of the sample (of cylindrical shape). This mechanism, termed here axial Biot–Gardner (BG) effect, depends not only on intrinsic properties of the rocks, like elastic moduli, permeability, but also on the length of sample and the dead volumes (Pimienta et al. 2016a, b; Sun et al. 2019). It is the axial version of the classical effect, where the flow takes place at the sides of the sample in the radial direction (Gardner 1962; White 1986; Dunn 1987). This theory was verified by Mörig and Burkhardt (1989) who made measurements in a paraffin-saturated sandstone, and observed experimentally that the relaxation peak shifts to higher frequencies with decreasing radius of the sample.

Regarding the sandstones, we consider only the intrinsic-loss mechanism, which is explained by the squirt-flow model and approximated with Zener mechanical elements (e.g., Carcione and Gurevich 2011), since the EIAS and CPEM

models consider unbounded media. On the other hand, Lavoux limestone has no cracks, only round pores of dual size, and therefore, the observed attenuation peak is due to the BG effect (open-drained conditions were implemented experimentally). In this case, a Zener fit is performed to test the relation between the quality factors obtained from the bulk and Young moduli, since experimental data of these two stiffnesses are available.

2 Models of Effective Stiffness Moduli and Attenuation

Let us assume a solid background medium containing spherical pores (1) and cracks (2), where the total porosity is ϕ . The background medium (grains) has the bulk and shear moduli K_s and μ_s , respectively. The voids can be dry or filled with a liquid of bulk modulus K_f and the cracks have an aspect ratio a . Moreover, let us define c and $1 - c$ as the crack and stiff-pore fractions, i.e., the fractions related to the soft and stiff porosities.

2.1 Relaxed and Unrelaxed Moduli

The poroelasticity theory provides expressions of the moduli based on Gassmann equations (Gassmann 1951; Mavko et al. 2009; Carcione 2014), without taking into account explicitly the aspect ratio and crack fraction. The Gassmann bulk and shear moduli are

$$K_G = \frac{K_s - K_m + \phi K_m (K_s/K_f - 1)}{1 - \phi - K_m/K_s + \phi K_s/K_f} \quad \text{and} \quad \mu_G = \mu_m, \quad (1)$$

where K_m and μ_m denote the dry-rock moduli, respectively. The Young modulus in isotropic media is given by

$$Y_G = \frac{9K_G\mu_G}{3K_G + \mu_G} \quad (2)$$

(Mavko et al. 2009, p. 23). These moduli correspond to the low-frequency limit or relaxed state.

The EIAS and CPEM models (Endres and Knight 1997; Adelinet et al. 2011) are illustrated in Appendices A and B, respectively. These models yield the low-frequency bulk and shear moduli, K_{com} and μ_{com} , and the high-frequency bulk and shear moduli, K_{iso} and μ_{iso} as a function of the aspect ratio and crack fraction, where the subscripts “com” and “iso” indicate fluid pressure communication and isolated pores through the pore space, respectively.

Both the EIAS and CPEM models have their root in the work of Eshelby (1957). The difference between the two models lies in the calculation of K_{com} . The CPEM model is directly based on Gassmann’s equations. The physics behind

these models is as follows. At low frequencies, the excess pressure is relieved and the fluid is isobaric at the scale of a representative elementary volume; thus Gassman equation applies. However, at high frequencies, the fluid is “frozen” and the pressure in the cracks is higher than the pressure in the pores ($K_{iso} > K_{com}$). This effect increases as the crack aspect ratio decreases. At the same aspect ratio, when stiff pores start to be replaced by cracks, K_{com} decreases much more rapidly than K_{iso} , but after a critical crack fraction, the dispersion decreases, because there is less pressure communication due to a decrease of stiff pores (Endres and Knight 1997). On the other hand, shear strains only affect the cracks (these are randomly oriented), since the spherical pores maintain their shape, and this is the reason of the monotonically increase in shear dispersion.

2.2 Extension to the Whole Frequency Range

The generalized Zener model (Carcione 2014, Sect. 2.4.5–6) can be used to describe the frequency dependence of dispersion and attenuation, when there are several loss mechanisms. The model satisfies the Kramers–Kronig relations (Carcione et al. 2018) and consists of a parallel connection of L Zener elements and, therefore, provides L relaxation peaks (up to two peaks are observed in the experimental data of the examples presented here). Let us assume that from the data we have M_0, M_∞, Q_{el} , and $f_l, l = 1, \dots, L$, corresponding to the relaxed and unrelaxed moduli, peak quality factor and relaxation frequency, respectively, where M represents any stiffness modulus, i.e., the bulk modulus K , the shear modulus μ , the Young modulus Y or the P-wave modulus E .

If we define the parameter $Q_l = Q_{el}/L$, an approximation of the complex modulus can be expressed as

$$M(f) = \frac{M_0}{L} \sum_{l=1}^L \frac{Q_l + i(f/f_l)(R_l + 1)}{Q_l + i(f/f_l)(R_l - 1)}, \tag{3}$$

$$R_l = \sqrt{1 + Q_l^2},$$

where $i = \sqrt{-1}$ and f is the frequency. The unrelaxed modulus ($f \rightarrow \infty$) is

$$M_\infty = \frac{M_0}{L} \sum_{l=1}^L \frac{R_l + 1}{R_l - 1}. \tag{4}$$

For one relaxation peak (one Zener element), it can be shown that the following relation between attenuation and dispersion holds,

$$Q = \frac{2\sqrt{M_\infty M_0}}{M_\infty - M_0}. \tag{5}$$

2.3 Dispersion, Phase Velocity and Quality Factor

The real modulus and quality factor are

$$M_r = \text{Re}(M) \quad \text{and} \quad Q_M = \frac{\text{Re}(M)}{\text{Im}(M)} \tag{6}$$

(Carcione 2014), respectively. If the P-wave modulus is

$$E = K + \frac{4}{3}\mu, \tag{7}$$

the phase velocities and quality factors are

$$c_p = \left[\text{Re} \left\{ \frac{1}{c} \right\} \right]^{-1} \tag{8}$$

and

$$Q = \frac{\text{Re}\{c^2\}}{\text{Im}\{c^2\}}, \tag{9}$$

respectively, where c denotes c_p or c_s , the complex and frequency-dependent P-wave and S-wave velocities

$$c_p = \sqrt{\frac{E}{\rho}} \quad \text{and} \quad c_s = \sqrt{\frac{\mu}{\rho}} \tag{10}$$

(Carcione 2014), respectively, where ρ is the mass density.

3 Examples

The experimental data can be found in Borgomano et al. (2017) (Lavoux limestone) and Pimienta et al. (2017) (Wilkenson and Bentheim sandstones) under either glycerine or water saturation. They provide data for the Young modulus, Y . Table 1 shows the micro-structural properties of these rocks. Wilkenson sandstone shows a large quantity of feldspars. Assuming bulk and shear moduli of 37.9 GPa and 44.3 GPa for quartz and 37.5 GPa and 15 GPa for feldspar, respectively, we obtain the properties reported in the table using the Hill average (Mavko et al. 2009). For Bentheim sandstone, we perform a similar calculation. For Lavoux limestone, we use the properties of calcite (Mavko et al. 2009) and the bulk modulus of glycerine is taken from Bridgman (1931).

3.1 Evaluating and Removing the Biot–Gardner Effect

The measurements used here, performed on cylindrical samples, are affected by the sample boundary effect (Pimienta et al. 2016a; Sun et al. 2019). The related attenuation is caused by drained (open-pore) or partially drained boundary

Table 1 Rock properties

Rock	ϕ (%)	κ (mD)	K_s (GPa)	μ_s (GPa)	K_f (GPa)	p_e (MPa)	Fluid	Minerals
Lavoux	23	10	77	32	4.36	2.5	Glycerine	ca (100 %)
Bentheim	24.8	500	37.9	43.1	2.5	1	Glycerine	qu-fe (98-2 %)
Bentheim	24.8	500	37.9	43.1	2.5	10	Glycerine	qu-fe (98-2 %)
Wilkenson	9.1	0.003	37.7	26.3	2.21	1	Water	qu-fe (51-49 %)
Wilkenson	9.1	0.003	37.7	26.3	2.21	2.5	Water	qu-fe (51-49 %)
Wilkenson	9.1	0.003	37.7	26.3	2.21	20	Water	qu-fe (51-49 %)

κ permeability, p_e effective pressure, *ca* calcite, *qu* quartz, *fe* feldspar

conditions and the generation of diffusion Biot modes at the ends of the sample, and is not due to the intrinsic attenuation of the rock. The fluid is allowed to flow axially out of the sample. Sealing the sample is not effective and may introduce additional loss mechanisms (Dunn 1987; Pimienta et al. 2016a).

This phenomenon is called here axial Biot–Gardner effect (Pimienta et al. 2016a, 2017) in analogy with the radial effect. The latter is quantified, for instance, by Eq. (3) in White (1986) and Eq. (9) in Johnson and Kostek (1995). Therefore, we have to distinguish between this effect and the peak related to the intrinsic dissipation given by the undrained/unrelaxed transition (squirt-flow loss in this case). Pimienta et al. (2016a, b) report the two peaks in quartz-pure Fontainebleau sandstones of low porosity. In particular, the peak observed in Lavoux limestone is solely due to the axial BG effect, so that in this case we merely apply the Zener fit, without using the EIAS and CPEM petrophysical models, to test the relation between the bulk and Young moduli quality factors. In addition, we also report the relaxation peak obtained from the radial and axial BG effects for comparison (see Appendices C and D for the relevant equations).

The sandstones have the two relaxation peaks, with the first (weaker) one corresponding to the axial BG effect, which is not described by the EIAS and CPEM models. The stronger peak corresponding to the undrained/unrelaxed transition is the local squirt-flow dissipation mechanism (Pimienta et al. 2017), well described by Zener elements (e.g., Carcione and Gurevich 2011). Since the amount of dispersion is higher than the actual intrinsic dispersion, because of the presence of the BG effect, we have to remove from the data the first peak (and the related dispersion). Figure 1 shows an example similar to that of Wilkenson sandstone at an effective pressure $p_e = 1$ MPa, presented below. The plot shows the dispersion (a) and dissipation factor (b) for the two peaks together (dots) and each single peak separately (solid lines). The parameters of the two peaks together (dots) are $Y_0 = 16.4$ GPa, $Y_\infty = 28.8$ GPa, $f_1 = 0.2$ Hz, $f_2 = 40$ Hz, $Q_1 = 15$ and $Q_2 = 2.25$. If the sample is perfectly sealed, the BG effect would disappear, and we should observe an increase in the Young modulus from the undrained regime

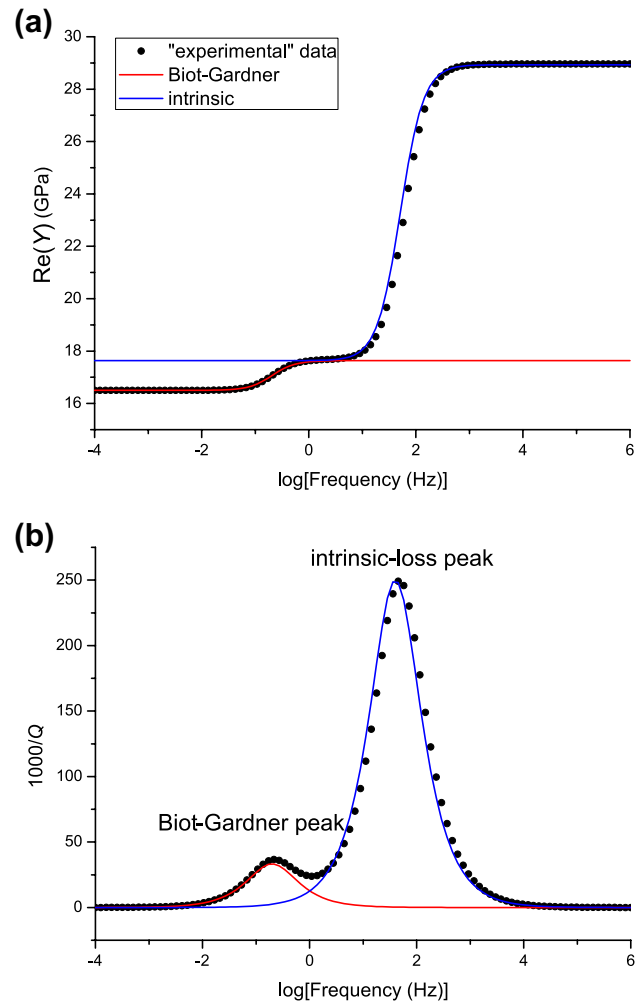


Fig. 1 Distinction between the Biot–Gardner and intrinsic losses. Dispersion (a) and dissipation factor (b) as a function of frequency. Two peaks together (dots) and each single peak (solid lines)

(when $\omega \rightarrow 0$) to the isolated regime ($\omega \rightarrow \infty$). The solid blue line representing the intrinsic squirt-flow peak has $Y_{\text{com}}(\text{exp}) = Y_0(R_1 + 1)/(R_1 - 1)$, i.e., the undrained (high-frequency limit) limit of the BG peak, with $Q_1 = 30$ and $Q_2 = 4$, which are approximately twice the previous quality factors (it is exactly twice for $Q \gg 1$). Basically, to capture

the second peak, one sets $Q_2 = Q_2(\text{exp}) = Q_{e2} = 4$ from the data (dots) and obtain the unrelaxed modulus as

$$Y_{\text{iso}}(\text{exp}) = Y_0 \cdot \frac{R_1 + 1}{R_1 - 1} \cdot \frac{R_2 + 1}{R_2 - 1}. \quad (11)$$

In this example, $Y_{\text{iso}}(\text{exp}) = 28.79$ GPa. The theoretical relaxed and unrelaxed Young moduli due to the intrinsic-loss peak are

$$Y_{\text{com}} = \frac{9K_{\text{com}}\mu_{\text{com}}}{3K_{\text{com}} + \mu_{\text{com}}} \quad \text{and} \quad Y_{\text{iso}} = \frac{9K_{\text{iso}}\mu_{\text{iso}}}{3K_{\text{iso}} + \mu_{\text{iso}}} \quad (12)$$

(Mavko et al. 2009), respectively.

3.2 The Dispersion Index

We define

$$D_K = \frac{K_{\text{iso}} - K_{\text{com}}}{K_{\text{com}}} \quad \text{and} \quad D_\mu = \frac{\mu_{\text{iso}} - \mu_{\text{com}}}{\mu_{\text{com}}} \quad (13)$$

as the normalized bulk and shear dispersion indices, respectively. Figure 2 shows the moduli (a) and dispersion indices (b) corresponding to Wilkenson sandstone at 1-MPa effective pressure and $a = 0.01$. The results are similar from a practical point of view, with the CPEM model predicting slightly higher values of the bulk modulus. There is no bulk dispersion at $c = 0$ and 1, while the shear dispersion increases from zero to a maximum at $c = 1$, as shown by Endres and Knight (1997) and Adelinet et al. (2011). When a single pore shape is present ($c = 0$ or 1), the incremental fluid pressure is the same at all pores, causing no bulk dispersion at these limits. For mixed pores shapes, the induced fluid pressure change in the cracks is greater than in the spheres and dispersion occurs. The dependence of D (for K) on the crack fraction has a maximum. The initial replacement of the spheres by cracks leads to a faster increase in pore space compressibility (because of pressure equilibration), compared to the isolated case. After the maximum (critical crack fraction), the decrease of equant pore space results in a smaller pressure gradient and D approaches zero at $c = 1$. However, the CPEM curves should be taken cautiously, since this model is based on a non-interactive approximation, unlike the EIAS model, i.e., low crack density.

3.3 Estimation of the Pore Structure

Fit of the experimental relaxed and unrelaxed moduli yields an estimation of the aspect ratio a and crack fraction c . It is not possible to invert for aspect ratio a and crack fraction c uniquely. We have the following set of non-linear equations with two unknowns to solve

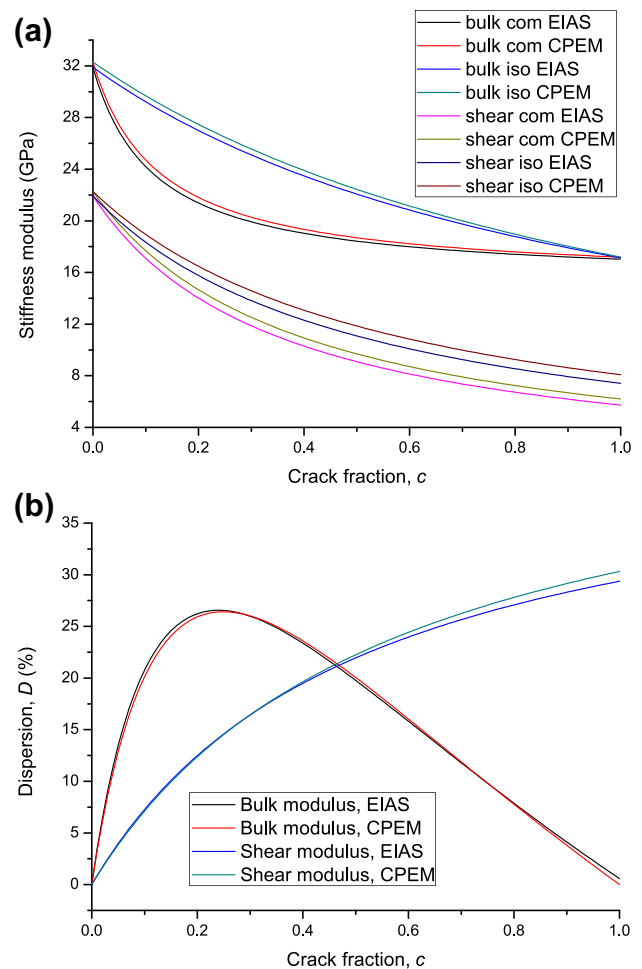


Fig. 2 Bulk and shear moduli (a) and bulk and shear dispersion, D_K and D_μ (b) as a function of the crack fraction, c , for an aspect ratio $a = 0.01$. The rock is Wilkenson sandstone (1-MPa effective pressure). The terms “com” and “iso” mean relaxed and unrelaxed, respectively

$$Y_{\text{com}}(a, c) = Y_{\text{com}}(\text{exp}) \quad (\omega \rightarrow 0), \quad Y_{\text{iso}}(a, c) = Y_{\text{iso}}(\text{exp}) \quad (\omega \rightarrow \infty), \quad (14)$$

where $Y_{\text{com}}(a, c)$ and $Y_{\text{iso}}(a, c)$ are given by Eq. (12), and “exp” refers to the experimental values. This type of equations may have no solution or several solutions. We span the range of physical solutions $a = [0, 0.1]$ and $c = [0, 0.1]$ and choose those satisfying

$$\left| 1 - \frac{Y_{\text{com}}(a, c)}{Y_{\text{com}}(\text{exp})} \right| + \left| 1 - \frac{Y_{\text{iso}}(a, c)}{Y_{\text{iso}}(\text{exp})} \right| \leq \epsilon, \quad (15)$$

with the minimum ϵ , but solutions with too small aspect ratios are to be avoided, since the shear modulus tends to zero for $a \rightarrow 0$.

Figures 3, 4, 5, 6 and 7 show the fit corresponding to the sandstones, and Tables 2 and 3 summarize the results, where, as indicated above (Fig. 1), we have fitted the second (intrinsic-loss) peak. For Wilkenson sandstone, we show the

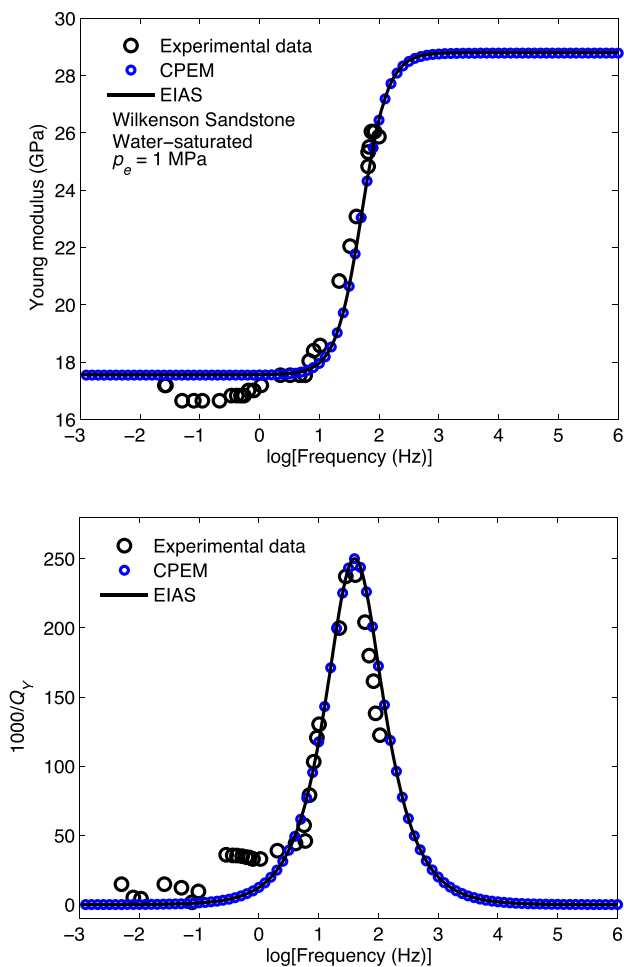


Fig. 3 Fit with the EIAS and CPEM models (black curve and blue circles) of the real part of the Young modulus, Y_r , and dissipation factor (inverse quality factor), $1000/Q_Y$, as a function of frequency, corresponding to Wilkenson sandstone ($p_e = 1$ MPa)

results of the EIAS and CPEM models (Figs. 3, 4 and 5). Tables 2 and 3 show that the aspect ratio decreases with increasing effective pressure, as expected, since the cracks tend to close. The crack fraction also decreases. The two models give similar results as can be expected from the comparison in Fig. 2, and the crack density of the EIAS model, computed with the stiffness moduli (see Appendix A) and not with the idealized expression (B.3) for ellipsoidal voids, is less than one. The results approximately agree with those of Pimienta et al. (2017). According to these authors, the average aspect ratio for Wilkenson sandstone is 0.0001 and that of Bentheim sandstones lies between 0.001 and 0.003. These estimations are based on the frequency of the relaxation peaks, assuming a squirt-flow attenuation mechanism. Moreover, the volumetric strain reported in Fig. 3 of Pimienta et al. (2017) indicates a variation from 0.012 to 0.2 (a relative variation of 17) between 1- and 20-MPa effective pressure for Wilkenson sandstone, similar to our results in

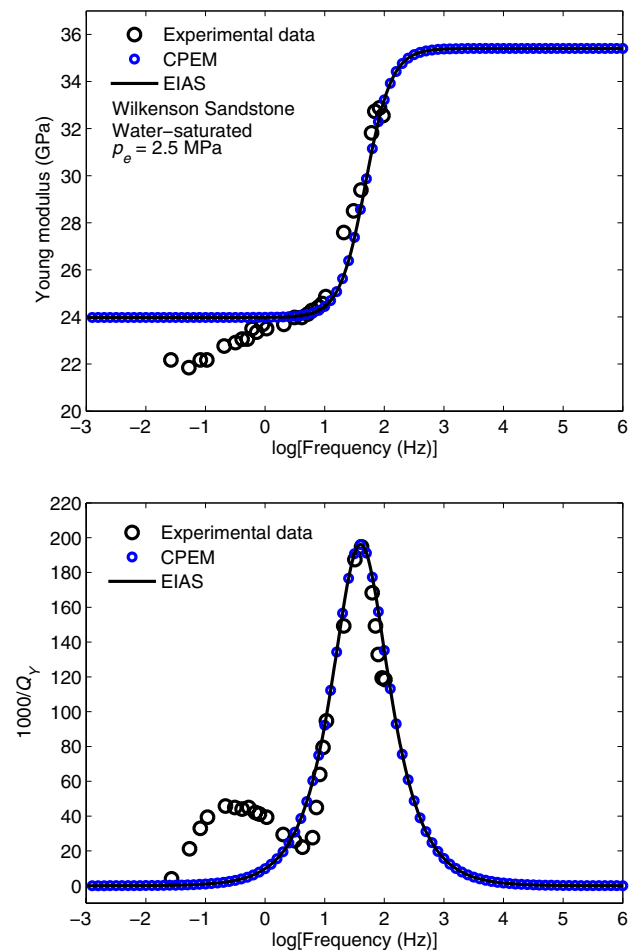


Fig. 4 Fit with the EIAS and CPEM models (black curve and blue circles) of the real part of the Young modulus, Y_r , and dissipation factor (inverse quality factor), $1000/Q_Y$, as a function of frequency, corresponding to Wilkenson sandstone ($p_e = 2.5$ MPa)

Table 2, where that relative variation for the soft porosity is 19.

We can also obtain the phase velocities and quality factors of the body waves. Let us consider Wilkenson sandstone at 1-MPa effective pressure. We calculate the complex bulk and shear moduli, K and μ as follows. We assume a medium with $K/\mu = K_{\text{com}}/\mu_{\text{com}} = \alpha$ at the optimal solution for a and c ($\alpha = 5/3$ for a Poisson medium, i.e., the Poisson ratio is 0.25). This is a strong assumption, because the Poisson ratio varies with frequency [from 0.24 to 0.37 according to Pimienta et al. (2017)]. A more accurate calculation requires the implementation of this variation. Then, we can express the P-wave modulus, E , and S-wave modulus, μ , as

$$E = \frac{(1 + 3\alpha)(4 + 3\alpha)}{27\alpha} \cdot Y \quad \text{and} \quad \mu = \frac{1 + 3\alpha}{9\alpha} \cdot Y, \quad (16)$$

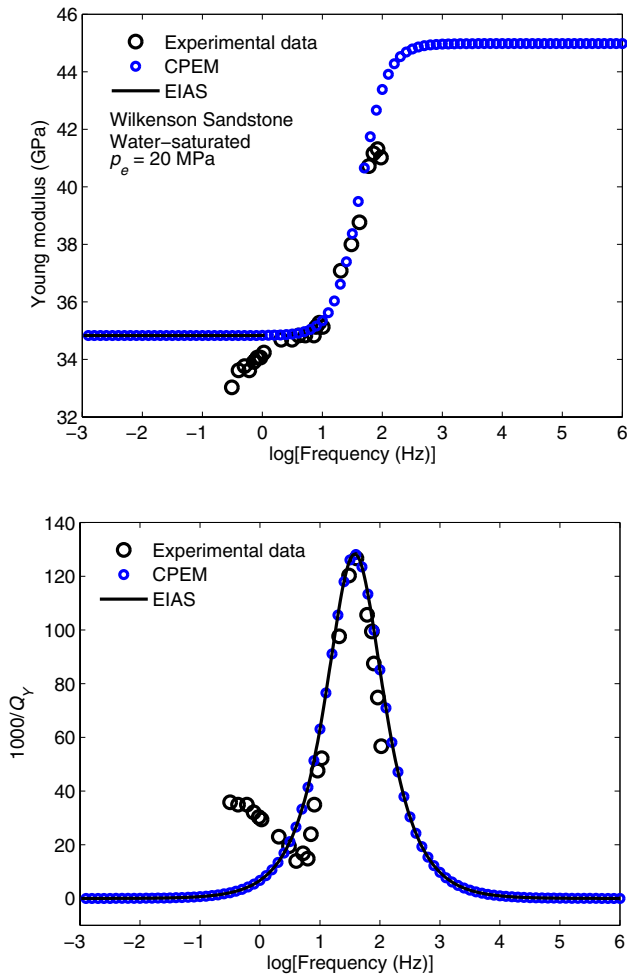


Fig. 5 Fit with the EIAS and CPEM models (black curve and blue circles) of the real part of the Young modulus, Y_r , and dissipation factor (inverse quality factor), $1000/Q_Y$, as a function of frequency, corresponding to Wilkenson sandstone ($p_e = 20$ MPa)

where Y is given by equation (3) (one Zener, the intrinsic loss). Figure 8 shows the phase velocities and dissipation factors. Since both waves have the same amount of dispersion, the relaxation peak is the same and equal to that of the Young modulus.

3.4 Matching the Biot–Gardner Effect

Figure 9 shows the fit of the data corresponding to Lavoux limestone with a Zener element, where K_0 is M_0 . We recall that this peak corresponds to the axial BG effect and the EIAS and CPEM models cannot be applied. In this case, we compute the theoretical Young modulus from the following equation:

$$Y(\omega) = \frac{9K(\omega)\mu}{3K(\omega) + \mu}, \tag{17}$$

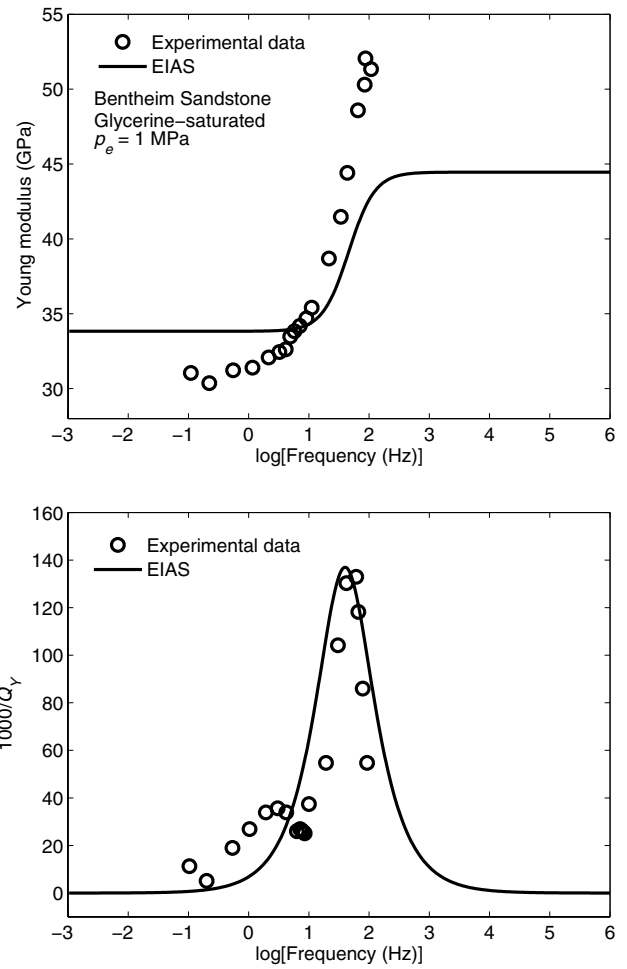


Fig. 6 Fit with the EIAS model of the real part of the Young modulus, Y_r , and dissipation factor (inverse quality factor), $1000/Q_Y$, as a function of frequency, corresponding to Bentheim sandstone ($p_e = 1$ MPa)

where $\mu = 8.75$ GPa (Borgomano et al. 2017, Fig. 10c), since there is no shear attenuation. Figure 10 compares the Young-modulus data (Borgomano et al. 2017, Fig. 9a, b) to the real modulus $Y_r = \text{Re}(Y)$ and quality factor Q_Y obtained from Eqs. (6) and (17) and those computed from the radial and axial BG effects [Eqs. (C.1), (D.9) (“drained”) and (D.11) (with a dead volume $V_d = 60$ mL) in appendices C and D]. The properties of Table 1 are used, and $K_m = 15$ GPa, $\mu = 8.94$ GPa, $\eta = 1$ Pa s, $L = 8$ cm and $r_0 = 2$ cm. While the Young modulus obtained with the Zener model and Eq. (17) has an excellent agreement, the theoretical expression of the axial BG effect is not matching the experimental data, mainly the location of the relaxation peak, while the level of attenuation is acceptable. Peculiarly, the radial BG equations provide a better fit, although the sample is sealed at the lateral boundaries. This problem is also addressed by Tan et al. (2019), using a modified Gassmann equation that takes into account the dead volume, and by Sun et al. (2019), who

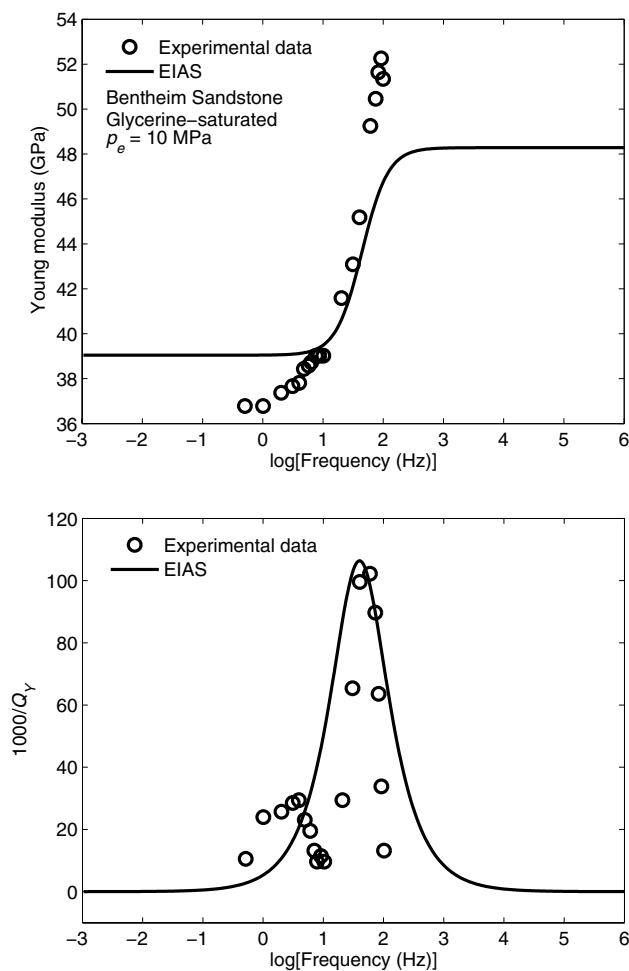


Fig. 7 Fit with the EIAS model of the real part of the Young modulus, Y_r , and dissipation factor (inverse quality factor), $1000/Q_y$, as a function of frequency, corresponding to Bentheim sandstone ($p_e = 10$ MPa)

established a 3D model. The cause of the discrepancy can be a partial radial flow at the sides of the sample that it is not taken into account by the 1D model and this is probably the reason why the radial effect provides a better fit.

4 Conclusions

We use the EIAS and CPEM models to obtain the aspect ratio and crack fraction from the Young-modulus dispersion, specifically from the low- and high-frequency limits. The models are extended to the whole frequency range on the basis of the Zener model, to describe intrinsic loss. The sandstone data follow the Kramers–Kronig relation, since the fit of the dispersion and quality-factor experimental data is satisfactory. Since the sandstone data suffer from the axial Biot–Gardner effect, the dispersion due to this mesoscopic-loss mechanism is removed. The aspect ratio decreases with increasing effective pressure, as expected, since the cracks tend to close, and the crack fraction also decreases. The two models give similar results.

Lavoux limestone has no cracks and the observed dispersion is solely due to the Biot–Gardner effect. In this case, we fit the bulk-modulus data with a Zener element and then compute the complex Young modulus. Its attributes are compared to the data and to the Biot–Gardner dispersion and quality-factor curves. The agreement with the experiment is excellent, when using the Zener model and the relation between the Young modulus and the bulk and shear moduli. However, the theoretical Biot–Gardner curves show some differences compared to the experimental data, with the radial one providing a better fit, possibly indicating that a component of radial flow is present and that the 1D axial theory cannot describe the data.

Table 2 EIAS results

Rock	p_e (MPa)	Y_{com} (GPa)	Y_{iso} (GPa)	a	c	ϵ
Wilkenson Sandstone	1	17.55	28.79	0.00105	0.0915	4.38×10^{-6}
Wilkenson Sandstone	2.5	23.98	35.41	0.00080	0.0433	4.52×10^{-7}
Wilkenson Sandstone	20	34.83	44.98	0.00021	0.0048	2.43×10^{-6}
Bentheim Sandstone	1	33.83	44.45	0.00215	0.0268	1.71×10^{-6}
Bentheim Sandstone	10	39.02	48.25	0.00165	0.0137	3.46×10^{-7}

Table 3 CPEM results

Rock	p_e (MPa)	Y_{com} (GPa)	Y_{iso} (GPa)	a	c	ϵ
Wilkenson Sandstone	1	17.55	28.79	0.00105	0.1014	1.83×10^{-6}
Wilkenson Sandstone	2.5	23.98	35.41	0.00092	0.0554	5.20×10^{-7}
Wilkenson Sandstone	20	34.83	44.98	0.00027	0.0069	9.35×10^{-7}

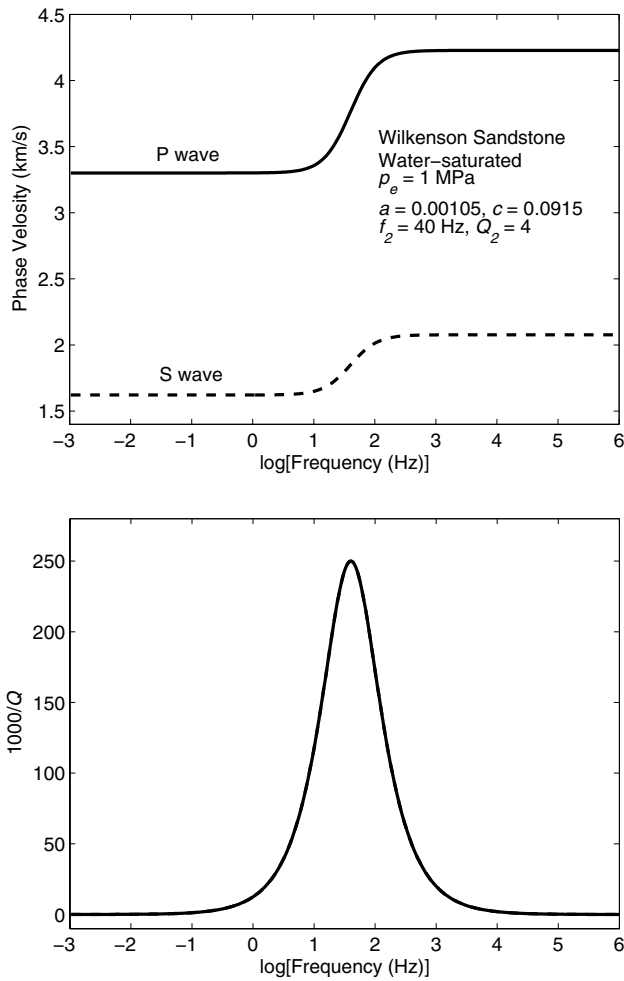


Fig. 8 Phase velocities and dissipation factors of the P and S waves, corresponding to Wilkenson sandstone ($p_e = 1$ MPa, EIAS fit). The dissipation factors of the two waves are the same

Acknowledgements We are grateful to two anonymous reviewers for detailed comments that highly improved the paper. This research was supported by The Cultivation Program of the “111 Plan”, China (Grant BC2018019), The Fundamental Research Funds for the Central Universities, China (Grant 2016B13114), National Natural Science Foundation of China (Grant 41974123, 41704109), Jiangsu Innovation and Entrepreneurship Plan, Specially-Appointed Professor Program of Jiangsu Province.

Compliance with Ethical Standards

Conflict of interest We declare that we do not have any commercial or associative interest that represents a conflict of interest in connection with this work.

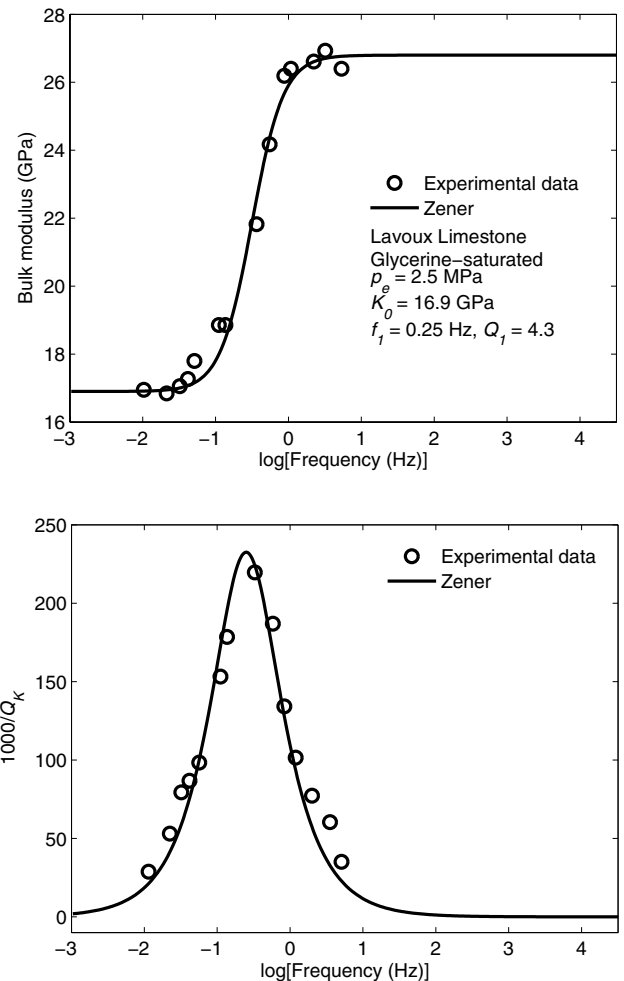


Fig. 9 Fit of the real part of the bulk modulus and dissipation factor (inverse quality factor), $1000/Q_K$, as a function of frequency, corresponding to Lavoux limestone

Appendix A: EIAS (Equivalent Inclusion-Average Stress) Model

The so-called isolated pores or high-frequency moduli, predicted by Endres and Knight (1997; Eqs. (32) and (33)), are

$$K_{iso} = K_s + \frac{\phi(K_f - K_s)\gamma}{1 - \phi(1 - \gamma)}, \tag{A.1}$$

$$\mu_{iso} = \frac{\mu_s(1 - \phi)}{1 - \phi(1 - \chi)},$$

where (Endres and Knight 1997; Eqs. (54) and (55)),

$$\gamma = (1 - c)P_1 + cP_2, \tag{A.2}$$

$$\chi = (1 - c)Q_1 + cQ_2$$

and (Berryman 1980a, b, 1995; Mavko et al. 2009, p. 187),

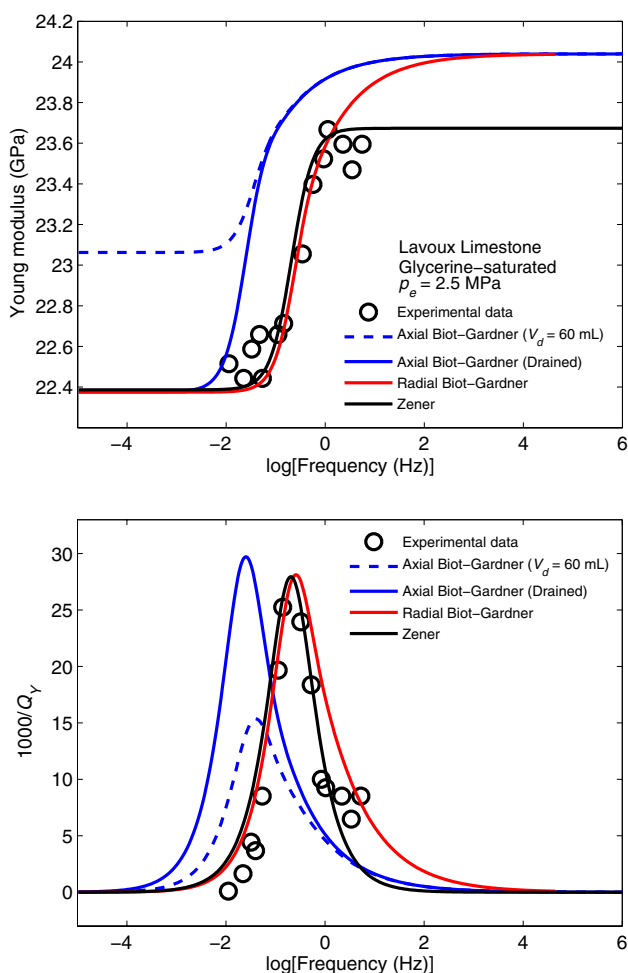


Fig. 10 Young modulus and related dissipation factor obtained with equation (17) (black line), the Biot–Gardner theory [red line (radial), equation (C.1); blue lines (axial), equations (D.9) (solid) and (D.11) (dashed)] and experimental data (open circles)

$$P_1 = \frac{K_s + 4\mu_s/3}{K_f + 4\mu_s/3},$$

$$P_2 = \frac{K_s}{K_f + \pi a \beta}, \quad \beta = \mu_s \cdot \frac{3K_s + \mu_s}{3K_s + 4\mu_s},$$

$$Q_1 = 1 + \mu_s/\zeta, \quad \zeta = \frac{\mu_s}{6} \cdot \frac{9K_s + 8\mu_s}{K_s + 2\mu_s},$$

$$Q_2 = \frac{1}{5} \left[1 + \frac{8\mu_s}{\pi a (\mu_s + 2\beta)} + 2 \cdot \frac{K_f + 2\mu_s/3}{K_f + \pi a \beta} \right],$$

(A.3)

where P_1 and Q_1 correspond to spherical pores and P_2 and Q_2 are approximations for penny-shaped cracks. Actually, there are (more complex) exact expressions for P and Q , which hold for any aspect ratio of the oblate spheroidal pores, including spherical pores and thin cracks: $P = \frac{1}{3} T_{ijj}$ and $Q = \frac{1}{5} (T_{ijj} - P)$, where T_{ijj} and T_{ijj} are given in Appendix A

of Berryman (1980b) or in page 189 of Mavko et al. (2009). The expressions P_1 and Q_1 for spherical pores are exact, while the approximations P_2 and Q_2 slightly deviate from the exact expressions at high aspect ratios of the cracks.

The effective moduli, when complete fluid pressure communication occurs (low frequencies), are (Endres and Knight 1997; Eqs. (34) and (35)),

$$K_{com} = K_s + \frac{\phi K_s (K_f - K_s) \gamma_0}{(1 - \phi)(K_s - K_f) + [K_f + \phi(K_s - K_f)] \gamma_0},$$

$$\mu_{com} = \frac{\mu_s (1 - \phi)}{1 - \phi(1 - \chi_0)},$$

(A.4)

where

$$\gamma_0 = (1 - c)P_{01} + cP_{02},$$

$$\chi_0 = (1 - c)Q_{01} + cQ_{02},$$

(A.5)

where

$$P_{01} = P_1(K_f = 0) = 1 + \frac{3K_s}{4\mu_s},$$

$$P_{02} = P_2(K_f = 0) = \frac{K_s}{\pi a \beta},$$

(A.6)

$$Q_{01} = Q_1(K_f = 0) = Q_1,$$

$$Q_{02} = Q_2(K_f = 0) = \frac{1}{5} \left[1 + \frac{4\mu_s}{\pi a} \cdot \frac{\mu_s + 8\beta}{3\beta(\mu_s + 2\beta)} \right].$$

The moduli K_{com} and μ_{com} [Eqs. (34) and (35) in Endres and Knight (1997)], with $K_f = 0$, are the dry-rock moduli to be used in Gassmann equations, i.e.,

$$K_{m0} = \frac{K_s(1 - \phi)}{1 + \phi(\gamma_0 - 1)}, \quad \mu_{m0} = \frac{\mu_s(1 - \phi)}{1 + \phi(\chi_0 - 1)},$$

(A.7)

since those moduli with $K_f \neq 0$ [equations (A.4)], are identical to the Gassmann moduli [Eqs. (52) and (53) in Endres and Knight (1997)]. Values of a and c can be obtained by fitting the relaxed and unrelaxed moduli.

The EIAS model has no restrictions on the crack density, since it considers the interactions between cracks. Endres and Knight (1997) also developed a dilute approximation given by their Eqs. (48)–(51), which shows a better agreement with the CPEM model (see next section) than the EIAS model.

For this model, we evaluate the crack density based on the stiffness moduli as in O’Connell and Budiansky (1974) and Budiansky and O’Connell (1976), which is summarized in page 187 of Mavko et al. (2009), identifying ν with the uncracked Poisson ratio (obtained from K_u and μ_u), and ν_{SC}^* with ν_{iso} (the same for the bulk modulus). The

uncracked wet-rock moduli K_u and μ_u are obtained from K_{iso} and μ_{iso} by setting the crack fraction $c = 0$.

Appendix B: CPEM (Cracks and Pores Effective Medium) Model

Adelinet et al. (2011) proposed alternative equations to the EIAS model, based on the non-interactive crack approximation, i.e., valid for low crack density. The high-frequency wet-rock moduli are obtained from

$$\frac{K_s}{K_{\text{iso}}} = 1 + \phi(1-c) \frac{3(1-\nu_s)}{2(1-2\nu_s)} \left(\frac{\delta_p}{1+\delta_p} \right) + \rho_c \frac{16(1-\nu_s^2)}{9(1-2\nu_s)} \left(\frac{\delta_c}{1+\delta_c} \right) \quad (\text{B.1})$$

and

$$\frac{\mu_s}{\mu_{\text{iso}}} = 1 + \phi(1-c) \frac{15(1-\nu_s)}{7-5\nu_s} + \rho_c \left[\frac{16(1-\nu_s)}{15(1-0.5\nu_s)} + \frac{32(1-\nu_s)}{45} \left(\frac{\delta_c}{1+\delta_c} \right) \right], \quad (\text{B.2})$$

where

$$\rho_c = \frac{3\phi c}{4\pi a} \quad (\text{B.3})$$

is the crack density,

$$\delta_p = \frac{2Y_s}{9(1-\nu_s)} \left(\frac{1}{K_f} - \frac{1}{K_s} \right), \quad \delta_c = \frac{\pi Y_s a}{4(1-\nu_s^2)} \left(\frac{1}{K_f} - \frac{1}{K_s} \right), \quad (\text{B.4})$$

and

$$Y_s = \frac{9K_s\mu_s}{3K_s + \mu_s} \quad \text{and} \quad \nu_s = \frac{3K_s - 2\mu_s}{2(3K_s + \mu_s)} \quad (\text{B.5})$$

are the mineral Young modulus and Poisson ratio, respectively.

The high-frequency dry-rock moduli can be obtained from equations (B.1) and (B.2) by taking $\delta_p \rightarrow \infty$ and $\delta_c \rightarrow \infty$, so that $\delta_p/(1+\delta_p) = 1$ and $\delta_c/(1+\delta_c) = 1$. The low-frequency wet-rock moduli K_{com} and μ_{com} are given by Gassmann equations (1), where K_m and μ_m are the high-frequency dry-rock moduli previously obtained.

Appendix C: The Radial Biot–Gardner Effect

White (1986) [Eq. (3)] reports the complex Young modulus related to the Biot–Gardner effect,

$$Y = 4\mu \cdot \frac{U - \Theta^*}{V - \Theta^*}, \quad \Theta = \frac{2J_1(x)}{xJ_0(x)}, \quad x = i^{5/2} r_0 \sqrt{\omega q}, \quad (\text{C.1})$$

where J_n are Bessel functions, r_0 is the radius of the cylinder,

$$U = \frac{(3W/4)(D+4/3)}{W-D}, \quad V = \frac{(W+1/3)(D+4/3)}{W-D}, \quad (\text{C.2})$$

$$W = \frac{K_G}{\mu}, \quad D = \frac{K_m}{\mu},$$

$$q = \frac{bH}{RP - Q^2}, \quad (\text{C.3})$$

$$H = P + R + 2Q = K_G + 4\mu/3, \quad K_G = K_m + \alpha^2 M,$$

$$P = K_m + (\alpha - \phi)^2 M + \frac{4}{3}\mu, \quad Q = \phi M(\alpha - \phi), \quad R = \phi^2 M,$$

$$M = \frac{K_s}{1 - \phi - K_m/K_s + \phi K_s/K_f}, \quad \alpha = 1 - \frac{K_m}{K_s},$$

$$b = \frac{\eta \phi^2}{\kappa}, \quad (\text{C.4})$$

η is the fluid viscosity and κ is the permeability [see Eqs. (2.20) and (3.3) in Gardner (1982), and Eqs. (7.16)–(7.18) in Carcione (2014)]. The factor $i^{5/2}$, instead of $i^{3/2}$, in the argument of the Bessel functions is due to the fact that we use here the opposite sign convention for the Fourier transform ($\omega \rightarrow -\omega$).

The theory predicts a relaxation frequency of

$$f_{BG} \propto \frac{\kappa K_m}{\eta} \quad (\text{C.5})$$

(Pimienta et al. 2017).

Appendix D: The Axial Biot–Gardner Effect

Pimienta et al. (2016a) obtained the Skempton coefficient and bulk modulus in the case that the rock sample satisfies open (“drained”) and semi-open boundary conditions at the ends, contrary to the Biot–Gardner theory, which holds for open conditions at the sides of the cylindrical sample (Gardner 1962; White 1986; Dunn 1987).

The Young modulus is

$$Y(\omega) = \frac{9K(\omega)\mu}{3K(\omega) + \mu}, \quad (\text{D.1})$$

where μ is assumed to be a real quantity and, according to Eqs. (9) and (11) in Pimienta et al. (2016a), the bulk modulus is

$$K(\omega) = \frac{LK_m}{B} \left[L(B^{-1} - \alpha) + \alpha \int_0^L f(\omega, z) dz \right]^{-1}, \quad (\text{D.2})$$

where

$$f(\omega, z) = \frac{\sinh[k(L-z)] + \sinh(kz)}{\sinh(kL)}, \quad k = (1+i)\sqrt{\frac{\omega}{2D}}. \quad (\text{D.3})$$

The various quantities are as follow: z is the axial spatial variable, L is the length of the sample,

$$B = \frac{\alpha M}{K_G}, \quad (\text{D.4})$$

is the Skempton coefficient.

$$M = \frac{K_s}{1 - \phi - K_m/K_s + \phi K_s/K_f}, \quad \alpha = 1 - \frac{K_m}{K_s}, \quad (\text{D.5})$$

are the fluid modulus and Biot coefficient, respectively,

$$K_G = K_m + \alpha^2 M, \quad (\text{D.6})$$

is the Gassmann bulk modulus,

$$D = \frac{\kappa}{S\eta} \quad (\text{D.7})$$

is the hydraulic diffusivity,

$$S = \frac{\alpha}{BK_m} \quad (\text{D.8})$$

is the storage coefficient, η is the fluid viscosity and κ is the permeability. Performing the integration in Equation (D.2), we obtain

$$K(\omega) = \frac{LK_m}{B} \left[L(B^{-1} - \alpha) + \frac{2\alpha[\cosh(kL) - 1]}{k \sinh(kL)} \right]^{-1}. \quad (\text{D.9})$$

In real experiments, the “drained” condition is difficult to achieve, Pimienta et al. (2016a) combined the purely drained and undrained conditions, and obtained the more realistic “experimentally undrained” condition. An approximate solution for the pressure p_f is given by their Eq. (15) (see also Sun et al. 2019), which holds for equal dead volumes on both ends of the sample. Since the local volumetric strain is $\epsilon_v = (1/K_m)(P - \alpha p_f)$, where P is the applied source pressure, it can be shown that we obtain Eq. (D.2) with

$$f(\omega, z) = \frac{\cosh[k(L/2 - z)]}{b \sinh(kL/2) + \cosh(kL/2)}, \quad b = \frac{2\pi r_0^2 S}{k S_V}, \quad (\text{D.10})$$

where $S_V = V_d/K_f$ is the storage capacity of the total dead volume, with V_d the dead volume and r_0 the radius of the

rock sample [see Borgomano et al. (2017) for values of the dead volume and other properties (below their Eq. (28))].

Performing the integration of equation (D10) as above [see equation (D2)], we obtain

$$K(\omega) = \frac{LK_m}{B} \left[L(B^{-1} - \alpha) + \frac{(2\alpha/k)}{b + \coth(kL/2)} \right]^{-1}. \quad (\text{D.11})$$

If $b \rightarrow 0$ (e.g., infinite dead volume), equations (D.9) and (D.11) coincide.

Sun et al. (2019) developed the theory in three dimensions, basically showing that in this case the peak frequency is lower than that predicted by the theory of Pimienta et al. (2016a), which indicates that the fluid flow needs more time to equilibrate the pore pressure.

References

- Adelinet M, Fortin J, Guéguen Y (2011) Dispersion of elastic moduli in a porous-cracked rock: theoretical predictions for squirt flow. *Tectonophysics* 503(1):173–181
- Benveniste Y (1987) A new approach to the application of Mori-Tanaka's theory in composite materials. *Mech Mater* 6:147–157
- Berryman JG (1980a) Long-wavelength propagation in composite elastic media I. Spherical inclusions. *J Acoust Soc Am* 68:1809–1819
- Berryman JG (1980b) Long-wavelength propagation in composite elastic media II. Ellipsoidal inclusions. *J Acoust Soc Am* 68:1820–1831
- Berryman JG (1995) Mixture theories for rock properties. *Rock physics and phase relations. Handbook Phys Constant* 3:205–228
- Borgomano JVM, Pimienta L, Fortin J, Gueguén Y (2017) Dispersion and attenuation measurements of the elastic moduli of a dual-porosity limestone. *J Geophys Res Solid Earth* 122(4):2690–2711
- Bridgman PW (1931) The volume of eighteen liquids as a function of pressure and temperature. *Proc Am Acad Arts Sci* 66(5):185–233
- Budiansky B, O'Connell R (1976) Elastic moduli of a cracked solid. *Int J Solids Struct* 13:81–97
- Budiansky B, O'Connell R (1980) Bulk dissipation in heterogeneous media. *Solid Earth Geophys Geotechnol* 42:1–10
- Carcione JM (2014) *Wave Fields in Real Media. Theory and numerical simulation of wave propagation in anisotropic, anelastic, porous and electromagnetic media*, 3rd edn. Elsevier, Amsterdam
- Carcione JM, Cavallini F, Ba J, Cheng W, Qadrouh A (2018) On the Kramers-Kronig relations, *Rheol. Acta*, <https://doi.org/10.1007/s00397-018-1119-3>
- Carcione JM, Gurevich B (2011) Differential form and numerical implementation of Biot's poroelasticity equations with squirt dissipation. *Geophysics* 76:N55–N64
- Carcione JM, Morency C, Santos JE (2010) Computational poroelasticity. A review. *Geophysics* 75:A229–A243
- Endres A, Knight R (1997) Incorporating pore geometry and fluid pressure communication into modeling the elastic behavior of porous rock. *Geophysics* 62(106):106–117
- Eshelby JD (1957) The determination of the elastic field of an ellipsoidal inclusion, and related problems. *Proc Roy Soc Lond Ser A* 241:376–396
- Dunn K-J (1987) Sample boundary effect in acoustic attenuation of fluid-saturated porous cylinders. *J Acoust Soc Am* 81(5):1259–1266
- Gardner G (1962) Extensional waves in fluid-saturated porous cylinders. *J Acoust Soc Am* 34(1):36–40

- Gassmann F (1951) Über die elastizität poröser medien. *Vierteljahresschrift der Naturforschenden. Gesellschaft in Zurich* 96:1–23
- Giraud A, Sevostianov I (2013) Micromechanical modeling of the effective elastic properties of oolitic limestone. *Int J Rock Mech Min Sci* 62:23–27
- Johnson DL, Kostek S (1995) A limitation of the Biot-Gardner theory of extensional waves in fluid-saturated porous cylinders. *J Acoust Soc Am* 97(2):741–744
- Jones TD (1986) Pore fluids and frequency-dependent wave propagation in rocks. *Geophysics* 51:1939–1953
- Kuster G, Töksoz M (1974) Velocity and attenuation of seismic waves in two phases media: part I. Theoretical formulations. *Geophysics* 39:587–606
- Mavko G, Mukerji T, Dvorkin J (2009) *The rock physics handbook*. Cambridge Univ. Press, Cambridge
- Mörig R, Burkhardt H (1989) Experimental evidence for the Biot-Gardner theory. *Geophysics* 54:524–527
- Müller TM, Gurevich B, Lebedev M (2010) Seismic wave attenuation and dispersion resulting from wave-induced flow in porous rocks—a review. *Geophysics* 75(5):75A147–75A164
- O’Connell RJ, Budiansky B (1974) Seismic velocities in dry and saturated cracked solids. *J Geophys Res* 79:4626–4627
- Pimienta L, Borgomano JVM, Fortin J, Gueguén Y (2016a) Modelling the drained/undrained transition: effect of the measuring method and the boundary conditions. *Geophys Prosp* 64(4):1098. <https://doi.org/10.1111/1365-2478.12390>
- Pimienta L, Fortin J, Borgomano JVM, Gueguén Y (2016b) Dispersions and attenuations in a fully saturated sandstone: experimental evidence for fluid flows at different scales. *Lead Edge* 35(6):495–501
- Pimienta L, Borgomano JVM, Fortin J, Gueguén Y (2017) Elastic dispersion and attenuation in fully-saturated sandstones: Role of mineral content, porosity and pressures. *J Geophys Res Solid Earth*. <https://doi.org/10.1002/2017JB014645>
- Sun C, Tang G, Zhao J, Zhao L, Long T, Li M, Wang S (2019) Three-dimensional numerical modelling of the drained/undrained transition for frequency-dependent elastic moduli and attenuation. *Geophys J Int* 219:27–38
- Tan W, Mikhaltsevitch V, Lebedev M, Glubokovskikh S, Gurevich G (2019) The sample boundary effect in the low-frequency measurements of the elastic moduli of rocks. *ASEG Extended Abstracts* 1:1–3. <https://doi.org/10.1080/22020586.2019.12073061>
- White JE (1986) Biot-Gardner theory of extensional waves in porous rods. *Geophysics* 54:524–527
- Zhang L, Ba J, Carcione JM, Sun W (2019) Modeling wave propagation in cracked porous media with penny-shaped inclusions. *Geophysics* 84(4):1–11

Publisher’s Note Springer Nature remains neutral with regard to jurisdictional claims in published maps and institutional affiliations.